PCCP

PAPER

View Article Online
View Journal | View Issue

Cite this: *Phys. Chem. Chem. Phys.*, 2022, **24**, 21872

Expansion of the multifunctionality in off-stoichiometric manganites using post-annealing and high pressure: physical and electrochemical studies†

Zhiwei Gong,[a] Wei Xu,[b] N. A. Liedienov,[ac]* D. S. Butenko,[d] I. V. Zatovsky,[ef]* I. A. Gural'skiy,[g] Ziyu Wei,[h] Quanjun Li,[a] Bingbing Liu,[a] Yu. A. Batman,[i] A. V. Pashchenko[acj] and G. G. Levchenko[ac]*

Prospects for the use of manganites in various areas of modern technologies require comprehensive studies of their physical and chemical properties. $La_{0.9}Mn_{1.1}O_3$ (LMO) ceramics have been synthesized at an annealing temperature t_{ann} of 1150 °C with further post-annealing at 1250, 1350, and 1450 °C. As t_{ann} increases, the structure symmetry changes, and both the crystallite size and chemical defects increase. The post-annealing, on one hand, leads to a dramatic reduction of the magnetocaloric effect (MCE) $|-\Delta S_M^{max}|$ from 3.50 to 0.75 J (kg K)$^{-1}$ at 2 T and a Curie temperature T_C from 227 to 113 K with increasing t_{ann}. On the other hand, an external hydrostatic high-pressure P works oppositely enhancing ferromagnetic interactions. The saturation of $-\Delta S_M^{max}$ and T_C is already achieved at a relatively low P of ≈ 0.4 GPa. LMO-1150 exhibits the best magnetocaloric characteristics compared with other studied samples. Moreover, the electrochemical characteristics of the LMO materials as electrocatalysts for overall water splitting (OER process) and features of their transformation in different 0.5 M K_2SO_4, 0.5 M K_2HPO_4, and 0.1 M $K_2B_4O_7$ electrolytes have been studied thoroughly. After electrocatalysis of LMO, the magnetization M decreases and T_C remains, which makes it possible to control the depletion of electrodes and predict their working time based on the magnetic measurements. All samples show the best OER activity in the 0.5 M K_2HPO_4 media. The obtained results demonstrate the ways for controlling the MCE of LMO under changing internal and external conditions, and an evaluation of the possibilities for their OER applications in electrocatalysts.

Received 29th April 2022,
Accepted 27th July 2022

DOI: 10.1039/d2cp01959k

rsc.li/pccp

1. Introduction

Rare-earth perovskite manganites have been extensively studied in the past few decades owing to their easy chemical production and structural diversity, as well as colossal magnetoresistance and high magnetocaloric effect (MCE) near the Curie temperature T_C.[1–4] All these have significantly increased interest in them and promoted the search for ways of their potential practical applications in magnetic memory devices, batteries, fuel cells, transistors, spintronic and electronic devices, magnetic refrigerators, medicine for treating cancer, and drug delivery.[5–8] The recent development of new magnetic refrigeration technology based on the MCE has become an alternative green and environmentally friendly approach compared to the conventional gas compression technique.[9,10] Among potential candidates for magnetic refrigeration, manganites show a low production cost, high chemical stability, and simple preparation.[9,11] Moreover, Mn-containing perovskites are effective catalysts for the oxidation of organic compounds (alcohols, methane, toluene, *etc.*),[12–14] and electrocatalysts, including, for water splitting (oxygen evolution reaction).[15–17]

[a] *State Key Laboratory of Superhard Materials, International Center of Future Science, Jilin University, 130012, Changchun, China. E-mail: g-levch@ukr.net*
[b] *State Key Laboratory of Inorganic Synthesis and Preparative Chemistry, College of Chemistry, Jilin University, 130012, Changchun, China*
[c] *Donetsk Institute for Physics and Engineering named after O.O. Galkin, NASU, 03028, Kyiv, Ukraine. E-mail: nikita.ledenev.ssp@gmail.com*
[d] *Academy for Advanced Interdisciplinary Studies, Southern University of Science and Technology, 518055, Shenzhen, China*
[e] *College of Physics, Jilin University, 130012, Changchun, China. E-mail: zvigo@ukr.net*
[f] *F. D. Ovcharenko Institute of Biocolloidal Chemistry, NASU, 03142, Kyiv, Ukraine*
[g] *Taras Shevchenko National University of Kyiv, 01601, Kyiv, Ukraine*
[h] *College of Physics Science and Technology, Heilongjiang University, 150080, Harbin, China*
[i] *Bogomolets National Medical University, 01601, Kyiv, Ukraine*
[j] *Institute of Magnetism NASU and MESU, 03142, Kyiv, Ukraine*

† Electronic supplementary information (ESI) available: XRD, elemental composition, and XPS of the LMO ceramics; magnetic properties of the LMO ceramics; magnetic properties of the LMO-1150 ceramics at high pressure; and electrochemical properties of the LMO ceramics. See DOI: https://doi.org/10.1039/d2cp01959k

Therefore, perovskites are multifunctional compounds with the prospect of practical applications in various industries.[16,18] This implies the need for a comprehensive study of the functional properties of new materials based on the perovskites to expand their potential.

The strong interconnection between the transport and magnetic properties is observed in these metal oxide materials. The explanation for this implies the use of different models including the double exchange (DE) interaction, the Jahn–Teller effect,[19] the polaronic effect,[20] the phase separation,[21] and the critical phenomena.[22] Moreover, the importance of an additional multiple DE mechanism *via* a $Mn^{3+} \leftrightarrow O^{2-} \leftrightarrow Mn^{2+} \leftrightarrow O^{2-} \leftrightarrow Mn^{4+}$ path has been shown recently for explaining the magneto-transport properties of off-stoichiometric manganites.[23]

The creation of chemical defects in a perovskite structure can lead to an appearance and improvement of ferromagnetic (FM) properties, and the precise tuning of the MCE: the magnetic entropy change (ΔS_M) and Curie temperature (T_C). Anion vacancies $V^{(a)}$ in the oxygen sublattice $O_{3-\delta}$ weaken the DE, decrease T_C, and almost preserve the magnetic entropy.[24] Cation vacancies $V^{(c)}$ in the A-sublattice sufficiently influence the magneto-transport properties of manganites modifying Mn–O bond lengths and Mn–O–Mn bond angles, which are responsible for the strength of exchange interactions, and for the appearance of Mn^{2+} ions in the A-sites and an additional multiple FM DE interaction.[2,23,25–28]

In addition, a change in the content of Mn in the A- and B-sites by the substitution of other ions, creation of cation vacancies $V_B^{(c)}$ or introduction of overstoichiometric manganese also strongly influences the magneto-transport properties of manganites.[2,23,25,26,28–32] Introducing excess Mn in the A- and/or B-positions has a number of advantages since it brings to the completeness of the B-sublattice due to the existence of $V_B^{(c)}$ vacancies and significantly improves the magneto-resistance effect without lowering T_C;[33–36] increases the metal–insulator temperature;[28] enhances transport properties and the FM metallic state due to the appearance of Mn^{2+} ions in the A-sites, which have a half-filled conduction band crossing the Fermi level, and causes the multiple DE.[23] It also increases the T_C and MCE, for example, in $La_{0.67}Ca_{0.33}Mn_{1+\delta}O_3$ nanopowders with $-\Delta S_M = 2.94$ J kg^{-1} K^{-1} (5 T) at $T_C = 240$ K for $\delta = 0$ and $-\Delta S_M = 2.90$ J kg^{-1} K^{-1} (5 T) at $T_C = 248$ K for $\delta = 0.05$;[37] in $La_{0.8-x}Ag_{0.2}Mn_{1+x}O_3$ bulk with $-\Delta S_M = 2.40$ J kg^{-1} K^{-1} (1 T) at $T_C = 300$ K for $x = 0$,[38] and $-\Delta S_M = 2.46$ J kg^{-1} K^{-1} (1 T) at $T_C = 271$ K for $x = 0.1$,[3] and in $La_{0.8-x}Ag_{0.2}Mn_{1+x}O_3$ nanopowders with $-\Delta S_M = 0.96$ J kg^{-1} K^{-1} (2 T) at $T_C = 306$ K for $x = 0$,[39] and $-\Delta S_M = 2.03$ J kg^{-1} K^{-1} (1 T) at $T_C = 308$ K for $x = 0.2$.[22]

The concentration of point defects of the vacancy type can be controlled by an annealing process[24,36] that influences the internal chemical pressure modifying structural properties and, as a result, functional properties. Additionally, as is shown,[40] the external high hydrostatic pressure affects oppositely the structural parameters of manganites relative to the chemical pressure. All these show perspectives on the accurate control and possibilities of expanding their functional properties.

In addition to the unique physical properties of manganites suitable for use in modern electronics or medicine, they also demonstrate excellent chemical properties. For example, lanthanum–manganese perovskites can exhibit high electrocatalytic activity. To improve the catalytic properties of such electrodes, a simultaneous study of physical properties is relevant. The possibilities of changing the size of manganite particles and their effect on electrocatalytic properties are of great interest. Moreover, the contactless heating and cooling of manganites as electrodes will influence their reaction rate. In this regard, the study of the MCE or the effect of heating under an alternating electromagnetic field is of particular interest. This work presents the results of a parallel study of the electrochemical properties of $La_{0.9}Mn_{1.1}O_3$ manganites along with investigating changes in crystallite sizes, structural features, and thermal properties, as well as their interconnection. For this purpose, off-stoichiometric $La_{0.9}Mn_{1.1}O_{3-\delta}$ ceramic samples have been selected and synthesized due to the following reasons: (i) high reproducibility of the samples,[3,32,38] (ii) Mn-containing perovskites are effective catalysts,[18] (iii) this off-stoichiometric compound $0.9:1.1:3-\delta$ demonstrates the non-zero magnetization in contrast to the classical antiferromagnetic (AFM) one $1:1:3$,[41] (iv) they have one of the most stable perovskite crystal structure with a tolerance factor t of 0.946 closed to 1,[42] (v) the presence of cation vacancies at A-positions leads to the appearance of an additional magnetism from Mn^{2+} ions,[2,23,25–28] and (vi) the overstoichiometric manganese on B-sites improves the magneto-transport and magnetocaloric properties.[3,33–36,40] Thus, the structural, microstructural, magnetic, magnetocaloric, and electrochemical properties of $La_{0.9}Mn_{1.1}O_3$ ceramics depending on post-annealing and/or high hydrostatic pressure have been studied systematically.

2. Experimental section

2.1. Sample preparation

Off-stoichiometric manganite $La_{0.9}Mn_{1.1}O_3$ (LMO) polycrystalline samples were synthesized using a two-step solid-state reaction method.[43] The initial La_2O_3 (purity 99.9%, Aladdin) and Mn_3O_4 (purity 99.9%, Aladdin) oxide powders were mixed in a planetary mill using ZrO_2 balls for 2.5 h. The initial synthesis was carried out at temperatures t_{synth} of 900 °C (20 h) and 950 °C (20 h). The obtained mixture was compressed in the pellets with a diameter of $\frac{1}{4}''$ ($\approx$6.35 mm) and a thickness of about 2 mm at a pressure P of 200 MPa. The first series of samples were annealed at a temperature t_{ann} of 1150 °C (22 h). Afterward, some parts of these samples were additionally post-annealed at 1250 °C (20 h), then at 1350 °C (3.5 h), and finally at 1450 °C (3 h). The stabilization t_{ann} was 5–10 min. The sintering was carried out in a slow heating and cooling mode of 3 °C min^{-1} in air. All heating treatments were conducted using a KSL-1700X furnace with a PID automatic temperature control system equipped with a thermocouple type B. The obtained samples were named LMO-1150, LMO-1250, LMO-1350, and LMO-1450.

2.2. Characterization

The structure and phase composition of the studied ceramic samples were examined by X-ray diffraction (XRD) using a Rigaku D/max-2500 diffractometer with Cu-$K_{\alpha 1}$ radiation (λ = 0.15418 nm) at room temperature. The lattice parameters were obtained by Rietveld refinement using the GSAS-II software.[44,45] As a starting model for the Rietveld refinement, atomic coordinates of $LaMnO_3$ (PDF #96-152-1792) for hexagonal and (PDF #96-151-1154) orthorhombic types, and Mn_3O_4 (PDF #96-151-4237) for the spinel type were selected. The relative changes of the sample mass $\Delta m/m$ during sintering were tested using a thermogravimetric method.[42] The morphology and size of the grains as well as the chemical composition were studied by scanning electron microscopy (SEM) using an FEI Magellan 400 scanning electron microscope with an energy-dispersive X-ray spectroscopy (EDS) module. The distribution function of the grain size was obtained from the analysis of SEM images using the Nano Measure 1.2.5 software.[18] X-Ray photoelectron spectroscopy (XPS) measurements were performed using an ESCALAB 250 X-ray photoelectron spectrometer. The XPS spectra were fitted and analyzed using the OriginPro 2018 software. The background of the X-ray photoelectronic lines was cut using the Shirley method. The spectra were excited using monochromatized Al-K_α radiation. The state of the surfaces was monitored through the C1s line, allowing the calibration of the energy scales for all spectra. The C1s line binding energy was approximately 285 eV. The magnetic properties of the ceramics were tested using a Quantum Design SQUID MPMS 3 magnetometer in a DC scan mode with a sophisticated temperature and a magnetic field control. The temperature dependences of the magnetization $M(T)$ in a field of H = 50 Oe were measured in zero-field cooling (ZFC) and field cooling (FC) regimes at a rate of 1 K min^{-1} within the temperature range from 2 to 400 K and with an accuracy of $\pm$0.5 K. The demagnetizing factor N for all samples was taken zero due to their cylindrically prepared shape, the long side of which was parallel to the magnetic field. The isotherms of magnetization $M(H)$ were measured up to 30 kOe near the Curie temperature T_C with a step of ΔT = 2 K and an accuracy of $\pm$1 K to determine the MCE. It should be noted that the Curie temperature of the samples was measured several times and by different approaches including $M(T)$, $M(H)$, and $\Delta S_M(T)$ dependences. All defined values of T_C are in good agreement with each other within the error of the experiment. Additionally, the magnetic measurements at a high pressure up to $P \approx 0.6$ GPa were conducted using a piston-type pressure cell made of Ni–Cr–Al alloy.[40,46] Silicon oil of low viscosity DC 200 was used as a pressure medium. The pressure was measured using the pressure dependence of the superconducting transition temperature of high-purity lead.[47]

2.3. Electrode fabrication and electrochemical measurements

To manufacture electrodes, the samples were mixed with conductive carbon black (“Super P”) and polyvinylidene fluoride (used as a binder) in a weight ratio of 85 : 10 : 5, and N-methyl pyrrolidone was added to make an active paste. The electrodes were fabricated by coating strips of carbon fiber (HCP331N) with an active paste. Then, the electrodes were dried at 80 °C (24 h) in a vacuum oven. Each electrode with a thickness of $\approx$0.5 mm had a geometric working surface area of about 1 cm^2.

All electrochemical tests for the overall water splitting (OER) catalytic activity of the electrodes were carried out using an electrochemical analyzer/workstation (Model 760E, CH Instruments) with a three-electrode cell. Three types of electrolytes have been used for electrochemical research, namely aqueous solutions of K_2SO_4 (0.5 M), $K_2B_4O_7$ (0.1 M), and K_2HPO_4 (0.5 M). The platinum plate and Ag/AgCl electrodes were used as the cathode and reference electrodes, respectively. The potential measured against the Ag/AgCl electrode was converted according to the Nernst equation, RHE = $E_{vs.Ag/AgCl}$ + 0.197 + 0.0592 pH. Electrochemical impedance spectroscopy (EIS) was performed in a frequency range of 10^{-2}–10^5 Hz with an amplitude of 5 mV at the open circuit potential, and the equivalent circuit of the EIS data was fitted using the ZView software. Linear sweep voltammetry (LSV) curves were collected at a scan rate of 1 mV s^{-1} with iR compensation (90%), and chronopotentiometry (CP) was performed at a constant current density of 10 mA cm^{-2}.

3. Results and discussion

3.1. Structural properties

The XRD patterns of all LMO ceramics synthesized at different annealing temperatures t_{ann} are shown in Fig. 1. LMO-1150 has a rhombohedral crystal structure $R\bar{3}c$ (No. 167) with a small amount of impurity Mn_3O_4 (about 6 wt%), which is ferrimagnetic with a transition temperature of $\sim$50 K and does not affect the functional properties of manganites.[48] LMO-1250 (rhombohedral $R\bar{3}c$) and LMO-1450 (orthorhombic *Pnma*) ceramics were fully single-phase with a different type of symmetry. For the LMO-1350 sample, a mixture of orthorhombic (*Pnma*) and rhombohedral ($R\bar{3}c$) phases was found with contents of about 72 and 28 wt%, respectively.

All structural parameters of LMO are summarized in Table 1 and Table S1 in the ESI.† The lattice parameters and unit cell volume change non-monotonically with an increase in t_{ann} that is associated with the type of symmetry, inhomogeneous, local distortions, structural defects, *etc.* For LMO-1150 and LMO-1250 with the same rhombohedral $R\bar{3}c$ crystal structure, as well as for LMO-1350 including also the rhombohedral $R\bar{3}c$ phase, the volume increases with an increase in t_{ann} that is caused by the magnification of structural defects due to reducing the oxygen content.[49,50] Accordingly, at a higher t_{ann}, symmetry decreases from rhombohedral to orthorhombic. This assumption is also confirmed by the thermogravimetric data. As t_{ann} increases, the sample mass $|-\Delta m/m|$ increases from 0.73 to 2.32%. Additionally, the rate of perovskite structure distortion can be estimated through the tolerance factor $t = (R_A + R_O)/\sqrt{2}(R_B + R_O)$, where R_A, R_B, and R_O are the average ionic radii of the A-, B-, and O-sites, respectively. The tolerance factor is an important structural parameter, which reflects the local microscopic distortion of the ideal ABO_3 perovskite structure with t = 1,[43] and correlates

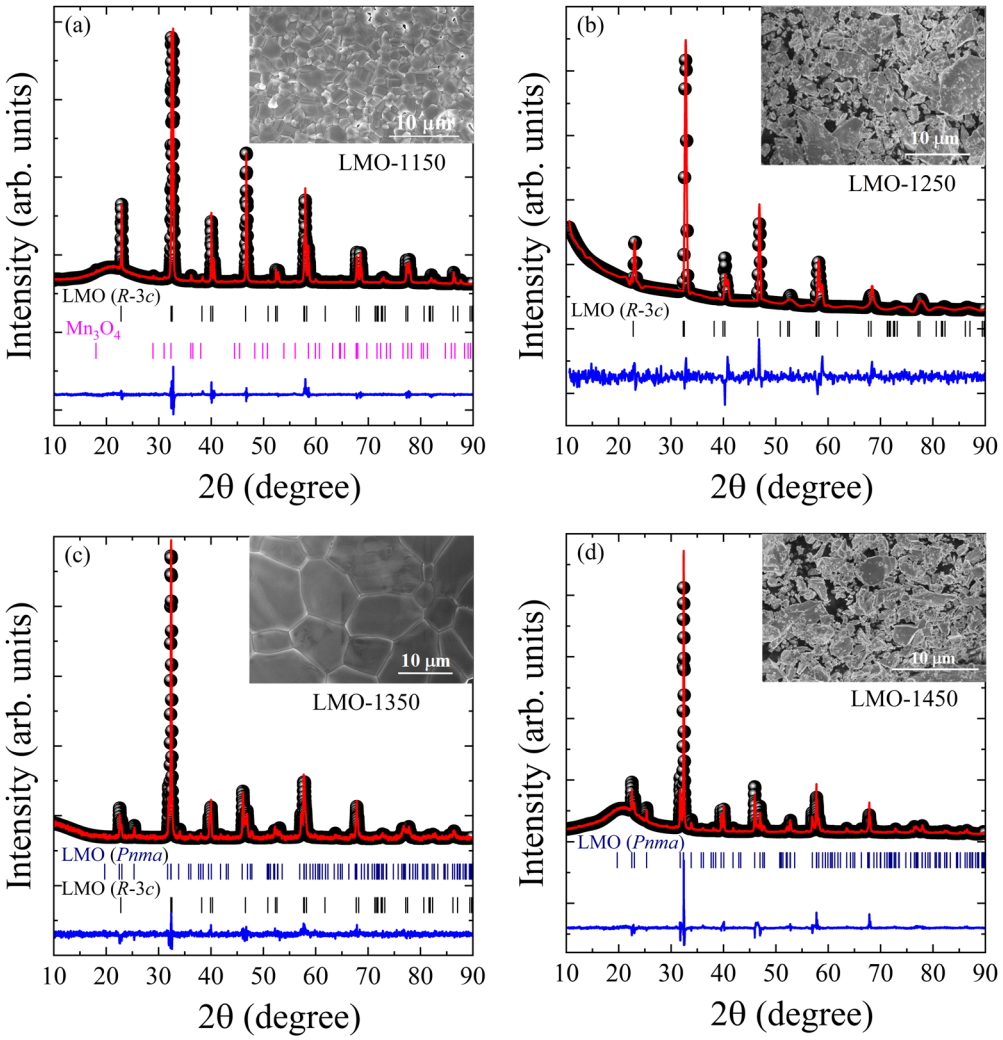

Fig. 1 XRD patterns of LMO measured at room temperature and fitted by the Rietveld method. The experimental (black cycles) and calculated values (upper red curves) and a difference curve (the bottom blue line) normalized to a statistical error are presented. Vertical bars are the calculated positions of diffraction peaks corresponding to the perovskite structures (rhombohedral $R\bar{3}c$ and orthorhombic *Pnma* types), and the presence of Mn_3O_4 second-phase for only LMO-1150. The insets are the SEM images.

Table 1 Phase composition, lattice parameters (*a*, *b*, *c*, and *V*), and agreement factors (R_p, R_{wp}, R_{exp}, and χ^2) of LMO at different t_{ann}

t_{ann}	1150 °C		1250 °C	1350 °C		1450 °C
Phase composition	LMO 93.9%	Mn_3O_4 6.1%	LMO 100%	LMO 72.3%	LMO 27.7%	LMO 100%
Space group	$R\bar{3}c$ (No. 167)	$I4_1/amd$ (No. 141)	$R\bar{3}c$ (No. 167)	*Pnma* (No. 62)	$R\bar{3}c$ (No. 167)	*Pnma* (No. 62)
a(Å)	5.52828(13)	5.759(2)	5.5289(20)	5.59693(25)	5.5206(29)	5.63238(24)
b(Å)				7.7461(3)		7.7280(3)
c(Å)	13.35899(18)	9.46(3)	13.417(4)	5.53264(31)	13.543(7)	5.52841(24)
V(Å^3)	353.578(11)	313.751(13)	355.19(13)	239.864(14)	357.45(9)	240.635(25)
R_{exp} (%)	4.24		9.52	2.89		3.76
R_p (%)	5.85		8.31	6.92		6.57
R_{wp} (%)	7.72		11.24	8.81		9.88
χ^2	3.34		1.43	9.37		6.97

with a change in the magnetic properties.[51] With an increase in the annealing temperature from 1150 to 1250, 1350, and 1450 °C, the tolerance factor *t* for all LMO reduces from 0.941 to 0.932, 0.923, and 0.919, respectively. For finding *t*, we used the Shannon radii,[52] the presence of Mn^{2+} ions, an electroneutrality principle, and the EDS data. The EDS (Fig. S1, ESI†) confirms approximately the stoichiometric ratio of LMO and correlates with the relative changes of the sample mass $\Delta m/m$

indicating the decrease in the oxygen content with an increase in t_{ann}. Moreover, as t_{ann} increases, the grain size of LMO increases from 1.6 to 8.1 μm which is also observed for deficient manganites.[53,54]

Additionally, XPS was used to define the surface elemental composition and valence state of the ions (Fig. 2 for Mn ions only and Fig. S2, ESI,† for others). It should be noted that La is trivalent in all considered compositions; however, the local charge of lanthanum is slightly different for rhombohedral (LMO-1150) and orthorhombic (LMO-1450) types (see the ESI†). This may be due to different La–O distances in these compounds. Accordingly, the XRD and XPS results are in good agreement. Mn2p spectra (Fig. 2(a)) show two main peaks at around 641 and 653 eV, which correspond to the $2P_{3/2}$ and $2P_{1/2}$ states, respectively. Mn2p spectra were decomposed into three components (Fig. 2(b and c)), which suggest the presence of three manganese Mn^{2+}, Mn^{3+}, and Mn^{4+} ions. The positions of their peak centers are listed in Table S2 (ESI†). With increasing t_{ann} and, consequently, defect chemistry, the ratio of Mn^{2+}/Mn^{3+}/Mn^{4+} varies from 21.9/45.9/32.2 for LMO-1150 to 26.7/44.4/28.9 for LMO-1450, showing the presence and increase of the Mn^{2+} concentration in the samples under study. It should be noted that the LMO-1450 spectrum is slightly shifted towards the lower energy relative to the LMO-1150 one, indicating an increase of the Mn^{2+} concentration in the more defect LMO-1450 sample. A similar behavior was observed earlier for non-defect LMO and La-defect L_dSMO samples with the increased content of Mn^{2+} in the last one.[25] Accordingly, the XPS results demonstrate that a part of Mn^{3+} ions undergoes charge disproportionation and multivalent forms of manganese occur for a series of prepared LMO samples, which should influence their magnetic and electrochemical properties.

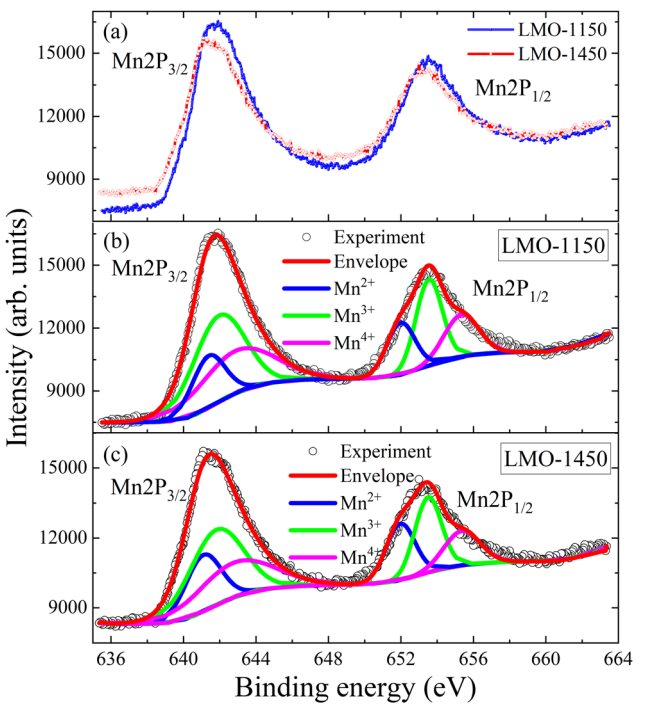

Fig. 2 Mn2p spectra (cycles) of LMO-1150 and LMO-1450 (a), and their fitting by the red envelope line and decomposition into Mn^{2+} (blue line), Mn^{3+} (green line) and Mn^{4+} (magenta line) components in LMO-1150 (b) and LMO-1450 (c).

3.2. Magnetic properties of the LMO ceramics

The temperature dependences of $M_{FC}(T)$ and $M_{ZFC}(T)$ at H = 50 Oe of all LMO were measured. The $M(T)$ curves display a FM–paramagnetic (PM) transition at T_C, which is determined from the minimum of dM/dT (see Fig. 3). LMO-1150 shows both the highest magnetization and T_C compared to other samples. Besides, t_{ann} affects adversely T_C. As t_{ann} increases, T_C reduces from 227 to 113–114 K. It is caused by several factors such as (i) a change in the type of the crystal structure from the $R\bar{3}c$ symmetry with isotropic MnO_6 octahedra (equal Mn–O bond lengths and Mn–O–Mn bond angles) for 1150 °C to the lower $P21/c$ symmetry with anisotropic MnO_6 octahedra (there are two different Mn–O bond lengths and three different Mn–O–Mn bond angles) for 1450 °C;[55] (ii) an increase in the structural defects confirmed bythe decreasing oxygen content from the XRD, thermogravimetric, and EDS data; and (iii) a magnification in the local distortions due to reducing t. All these lead to the weakening of the conventional DE $Mn^{3+} \leftrightarrow O^{2-} \leftrightarrow Mn^{4+}$ and multiple DE $Mn^{3+} \leftrightarrow O^{2-} \leftrightarrow Mn^{2+} \leftrightarrow O^{2-} \leftrightarrow Mn^{4+}$ interactions,[28] the appearance of additional antiferromagnetic (AFM) $Mn^{2+} \leftrightarrow O^{2-} \leftrightarrow Mn^{2+}$, $Mn^{4+} \leftrightarrow O^{2-} \leftrightarrow Mn^{2+}$, $Mn^{4+} \leftrightarrow O^{2-} \leftrightarrow Mn^{4+}$, and $Mn^{2+} \leftrightarrow O^{2-} \leftrightarrow Mn^{4+}$ interactions,[56–58] and a decrease in both the T_C and FM phase (see Fig. 3).

An inverse magnetic susceptibility $\chi^{-1}(T)$ deduced from the $M_{FC}(T)$ curve and its approximation are presented in Fig. 3. For all LMO in the PM phase at $T > T_C$, the temperature dependence of $\chi(T)$ satisfies the Curie–Weiss law $\chi = C/(T - \theta)$, where θ is the PM Curie temperature, $C = N\ \mu_{eff}{}^2/(3k_B)$ is the Curie constant with the number of PM manganese ions N, the effective magnetic moment of manganese μ_{eff} in Bohr magnetons μ_B, and the Boltzmann constant k_B. The theoretical effective magnetic moment μ_{eff}^{theor} can be calculated from $\mu_{eff}^{theor} = \sqrt{x_1\mu^2_{Mn^{2+}} + x_2\mu^2_{Mn^{3+}} + x_3\mu^2_{Mn^{4+}}}$, where x_1, x_2, and x_3 are the concentrations of Mn^{2+} with a magnetic moment $\mu_{Mn}{}^{2+}$ = 5.92 μ_B, Mn^{3+} with $\mu_{Mn}{}^{3+}$ = 4.90 μ_B, and Mn^{4+} with $\mu_{Mn}{}^{4+}$ = 3.87 μ_B for the ground state, respectively.[59] To calculate μ_{eff}^{theor}, we used an electroneutrality principle for the non-defect stoichiometric $\{La_{0.9}{}^{3+}Mn_{0.1}{}^{2+}\}_A[Mn_{0.9}{}^{3+}Mn_{0.1}{}^{4+}]_BO_3{}^{2-}$ composition. The experimental μ_{eff}^{exp} and theoretical μ_{eff}^{theor} as well as C and θ values are listed in Table 2. θ Shows the positive values for all LMO, which indicates the dominant FM interactions in them. The LMO-1150 sample is the most magnetically homogeneous, whereas other specimens indicate the Griffiths phase,[60–63] which exists from T_C to T_G and achieves the range of 173 K for LMO-1250, 167 K for LMO-1350, and 161 K for LMO-1450. All LMO demonstrate the increased values of μ_{eff}^{exp} compared to μ_{eff}^{theor}, which may be explained by the existence of short-range FM clusters and/or the localization of e_g-electrons on Mn-sites in the PM phase.[64,65]

The magnetic field dependences of magnetization $M(H)$ of the LMO ceramics at 2, 77, and 400 K are shown in Fig. 4.

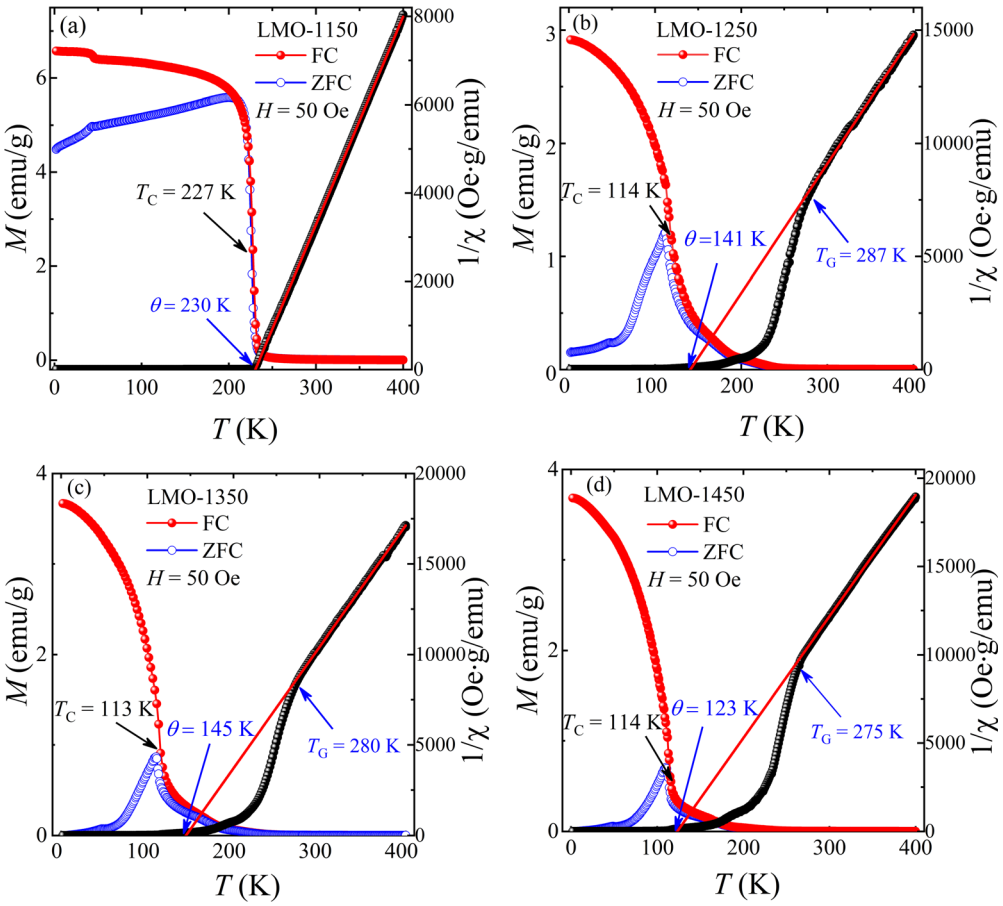

Fig. 3 $M_{FC}(T)$ and $M_{ZFC}(T)$ (red and blue cycles) at H = 50 Oe, and $\chi^{-1}(T) = H/M(T)$ (black cycles) and its approximation by the Curie–Weiss law (red line) of LMO-1150 (a), LMO-1250 (b), LMO-1350 (c), and LMO-1450 (d). θ is the PM Curie temperature.

Table 2 Magnetic moments μ calculated both experimentally and theoretically of LMO annealed at t_{ann}

			$T > T_C$ (PM state)		T = 2 K (FM state)	
t_{ann}	C (emu K/Oe g)	θ (K)	μ_{eff}^{exp} (μ_B)	μ_{eff}^{theor} (μ_B)	μ^{exp} (μ_B)	μ^{theor} (μ_B)
1150	0.021	230	5.97	4.90	2.86	4.00
1250	0.017	141	5.37	4.90	1.22	4.00
1350	0.015	145	5.04	4.90	0.89	4.00
1450	0.015	123	5.04	4.90	1.22	4.00

The main magnetic parameters obtained from the hysteresis curves $M(H)$ are presented in Tables 2 and 3. As t_{ann} increases, the magnetic moment μ^{exp} decreases and differs μ^{theor}, the saturation magnetization M_S decreases, whereas the coercivity H_C and the residual magnetization M_R increase. At 2 K, all samples, except LMO-1150, do not saturate even at 70 kOe (see Fig. 4(d)) indicating the competing interactions between the FM and AFM phases. There is also no saturation at 77 K. At 400 K, all LMO are in the PM state.

The isotherms of $M(H)$ around T_C with an interval of 2 K of all LMO ceramics are shown in Fig. S3 (ESI†). The temperature dependence of the magnetic entropy change $\Delta S_M(T, \mu_0 H)$ near T_C can be estimated using the Maxwell relationship:[66,67]

$$\Delta S_M(T, \mu_0 H) = S_M(T, \mu_0 H) - S_M(T, 0) = \int_0^{\mu_0 H} (\partial M/\partial T)_{\mu_0 H} d(\mu_0 H). \quad (1)$$

The 3D temperature and field dependences of $\Delta S_M(T, \mu_0 H)$ of all LMO are shown in Fig. 5. LMO-1150 shows the largest $\Delta S_M^{max} = -2.142$ J (kg K)$^{-1}$ under 1 T at T_C = 228 K among the studied ceramics under the same field and it is higher than that for similar lanthanum–manganese compounds (Table 4).[68–73] It makes them promising materials for practical applications with the possible adaptation for magnetic refrigerators, magnetic and electric field sensors, and nonlinear optical systems.[38,74,75] Such large values of the MCE in LMO-1150 exhibit an optimal order/disorder ratio caused by, on the one hand, the conventional DE *via* $Mn^{3+} \leftrightarrow O^{2-} \leftrightarrow Mn^{4+}$ and multiple DE *via* $Mn^{3+} \leftrightarrow O^{2-} \leftrightarrow Mn^{2+} \leftrightarrow O^{2-} \leftrightarrow Mn^{4+}$,[28] and, on the other hand, the structural defects and distortions.[40] In all other samples, the MCE decreases with an increase in t_{ann} due to the enlargement of structural heterogeneities. At the same time, the relative cooling power RCP = $|-\Delta S_M^{max}| \cdot \Delta T_{FWHM}$, where $-\Delta S_M^{max}$ is the maximum of entropy and ΔT_{FWHM} is the full width at half maximum, also reduces with the increasing t_{ann}.

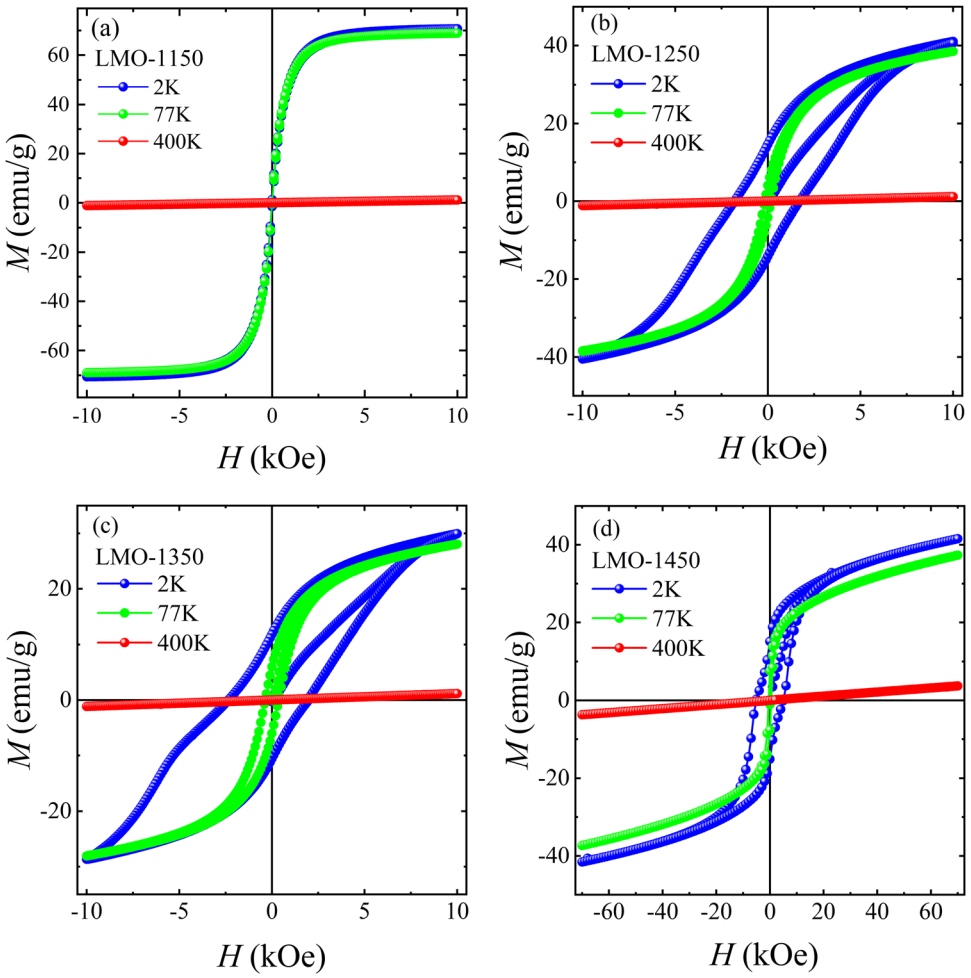

Fig. 4 Field dependences of $M(H)$ at 2, 77, and 400 K of LMO-1150 (a), LMO-1250 (b), LMO-1350 (c), and LMO-1450 (d).

Table 3 Saturation magnetization M_S, remnant magnetization M_R, and coercivity H_C of LMO annealed at different t_{ann}

	2 K			77 K	
t_{ann}	M_S (emu g^{-1})	M_R (emu g^{-1})	H_C (kOe)	M_R (emu g^{-1})	H_C (kOe)
1150	68.30	1.320	0.012	0.184	0.002
1250	29.27	14.625	1.798	4.068	0.165
1350	21.19	11.804	2.348	5.971	0.361
1450	29.21	15.200	5.000	7.690	0.476

3.3. Magnetic properties of the LMO-1150 ceramics at high pressures

Since LMO-1150 is the most perspective ceramic sample with the highest ΔS_M^{max} among the studied ones, additional research studies at the high hydrostatic pressure P were performed to establish the regularities between MCE parameters and P. Fig. 6 shows the temperature dependence of magnetization $M_{FC}(T)$ at different pressures P. Both ZFC and FC curves for each pressure are shown in Fig. S4 (ESI†). As P increases, both T_C and the FM phase increase achieving saturation at a relatively low P of $\approx$ 0.4 GPa. The maximum change in the Curie temperature is ΔT_C = 14 K.

Fig. 7 shows the 3D evolution of the magnetic entropy change $\Delta S_M(T, \mu_0 H)$ depending on the applied pressure obtained from the isothermal M–H curves (see Fig. S5, ESI†). As expected, ΔS_M exhibits a peak at around T_C where the fastest variation of magnetization with a temperature is observed. The temperature dependence of ΔS_M under pressure shows a similar shape as that at ambient pressure, but the peak position significantly moves to higher temperatures. In comparison with ambient pressure, the maximum of ΔS_M under pressure reduces slightly and also reaches saturation.

As shown in Fig. 8, T_C and ΔS_M increases and decreases linearly at a relatively low-pressure P of $\approx$ 0.4 GPa, respectively, and the pressure coefficient is $dT_C/dP \approx 31$ GPa. With a further increase in $P \geq$ 0.4 GPa, T_C and ΔS_M change very slowly achieving saturation at 241 K and 1.8 J kg^{-1} K^{-1}, respectively. A similar behavior was observed in $La_{0.7}Ca_{0.3}MnO_3$ under P.[85]

The obtained results demonstrate that the peak position of the MCE and the Curie temperature in the studied manganite ceramics can be effectively tuned by applying pressure. The effect of pressure on the T_C and MCE can be understood in terms of the pressure-tuned FM interaction.[86] It is well known that the conventional DE and also multiple DE interactions[40]

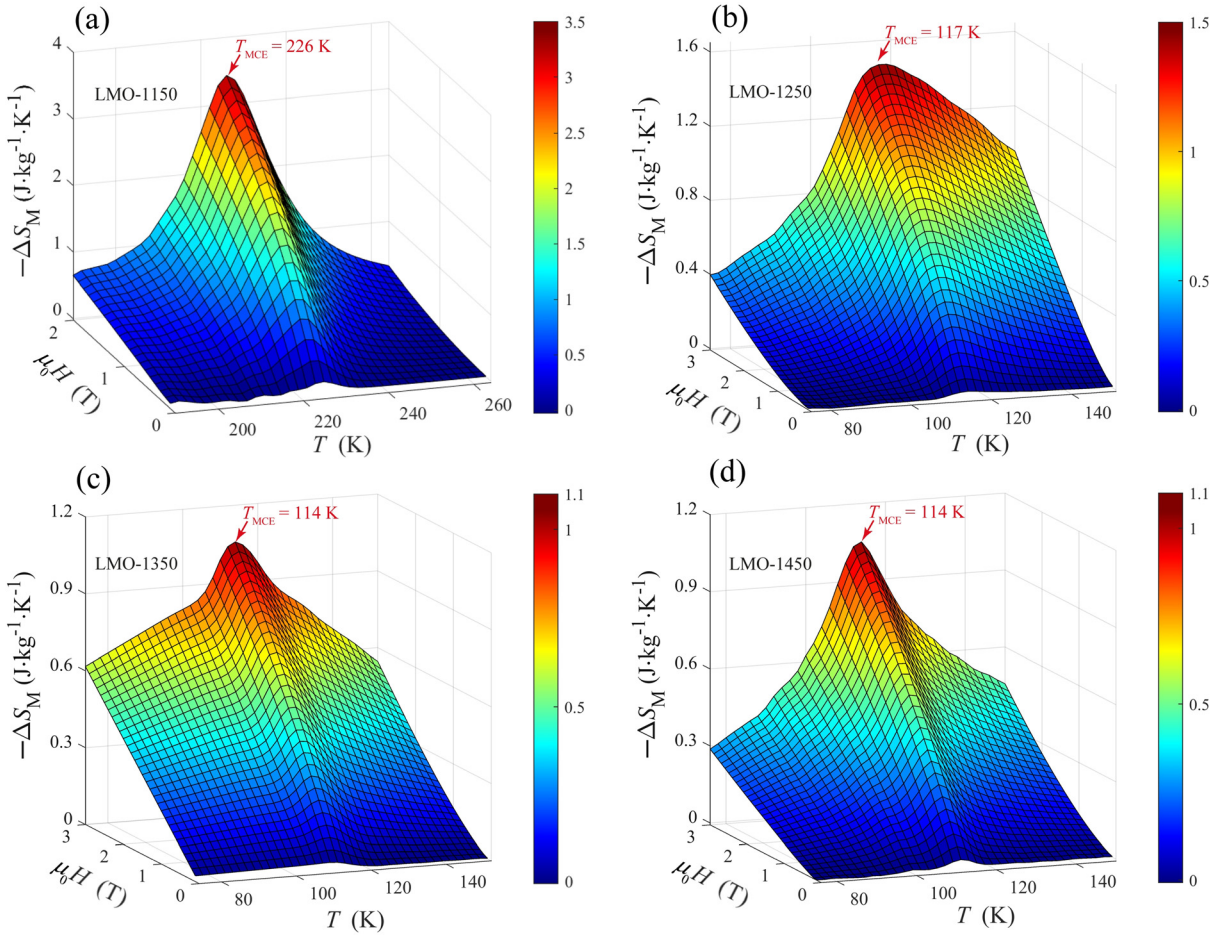

Fig. 5 Evolution of the magnetic entropy change $\Delta S_M(T, \mu_0 H)$ of LMO-1150 (a), LMO-1250 (b), LMO-1350 (c), and LMO-1450 (d).

depend on the lattice parameters through both the Mn–O–Mn angle θ and the Mn–O bond length d_{Mn-O}, as well as the strength of the spin-lattice coupling in these manganites. T_C is proportional to the e_g-electron bandwidth $T_C = \theta W = \beta \cos^2\theta/(d_{Mn-O})^{3.5}$, where β is a constant. Therefore, the increase in θ and the decrease in d_{Mn-O} caused by the pressure results in an increase in the W and, consequently a increase in T_C. As can be seen from Fig. 8, T_C reaches saturation at relatively low pressures which is supposed to be around $\theta = 180^\circ$. At the same time, the applied pressure suppresses the magnetic anisotropy enhancing the magnetization near T_C (see Fig. 6) and slightly decreasing the magnetic entropy change. The MCE strongly depends on the spin-lattice coupling in the magnetic ordering process, which is supposed to be decreased by the increasing applied pressure. Thus, an external hydrostatic pressure should increase the Mn–O–Mn angle toward 180° and decrease the Mn–O bond length.[83] Such lattice changes would be in favor of the DE and multiple DE interactions and, consequently, promote the magnetic ordering transition to higher temperatures, as shown recently for similar manganite compounds.[87]

3.4. Electrochemical properties of the LMO ceramics

Mn-containing perovskites can exhibit high electrocatalytic activity for overall water splitting.[88–93] Here, we have studied the electrochemical behavior of the prepared LMO samples as electrocatalysts for the OER process. It should be noted that the destruction of the catalyst may occur due to the conversion of manganese into high valence forms (Mn^{6+} or Mn^{7+}) when electrolysis is carried out in alkaline media. Therefore, testing was conducted using aqueous electrolytes with pH close to neutral values: 0.5 M K_2SO_4 (pH = 7.0), 0.5 M K_2HPO_4 (pH = 8.3), and 0.1 M $K_2B_4O_7$ (pH = 9.2).

In the first stage, the fabricated electrodes were placed in an electrolyte environment for 1 h, and then AC impedance spectroscopy was performed to assess the charge transfer process of materials in different mediums at the electrode–electrolyte interface. Fig. S6 (ESI†) presents the results of these measurements as the Nyquist plots. The impedance spectrum includes two parts for all electrolytes, a line in a low-frequency region and a semicircle in a high-frequency region. The EIS results correlate well with the equivalent circuit, which includes series resistance (R_s) and charge transfer resistance (R_{ct}) as shown in Fig. S7 (ESI†). R_s is obtained from the X-intercept yields of the Nyquist plot, and R_{ct} is determined by the diameter of the semicircle. The small R_s values contribute to the contact between the catalyst materials and substrate, while the R_{ct} values indicate a charge transfer of the catalyst–electrolyte.[94] It should be noted that the R_{ct} value is inversely proportional to the electrochemical activity of the material.[95] Accordingly, the

Table 4 Comparable data on the Curie temperature T_C, magnetic entropy change ΔS_M, and relative cooling power parameter RCP of manganites depending on the field $\mu_0\Delta H$ and high hydrostatic pressure P

Composition	T_C (K)	$\mu_0\Delta H$ (T)	P (GPa)	$-\Delta S_M^{max}$ (J kg^{-1} K^{-1})	RCP (J kg^{-1})
LMO (bulk)[present]	227	1	0	2.14	38.56
	241	1	0.6	1.79	32.67
LMO-1250 (bulk)[present]	114	1	0	0.56	22.28
LMO-1350 (bulk)[present]	113	1	0	0.41	13.77
LMO-1450 (bulk)[present]	114	1	0	0.40	9.50
$LaMnO_3$ (bulk)[70]	120	5	0	2.69	—
$LaMnO_3$ (bulk)[69]	124	5	0	2.69	250
$LaMnO_3$ (40 nm)[68]	260	5	0	4.02	241
$LaMnO_3$ (40 nm)[69]	150	5	0	2.40	250
$LaMnO_3$ (100 nm)[68]	256	5	0	6.36	245
$LaMnO_3$ (200 nm)[69]	135	5	0	2.67	355
$LaMn_{0.9}Fe_{0.1}O_3$ (bulk)[76]	136	1	0	1.20	48
$La_{0.8}K_{0.2}MnO_3$ (bulk)[77]	327	1	0	0.94	—
$La_{0.67}Sr_{0.33}MnO_3$ (bulk)[25]	364	1	0	1.62	—
$La_{0.58}\square_{0.09}Sr_{0.33}MnO_3$ (bulk)[25]	360	1	0	1.41	—
$La_{0.67}Sr_{0.24}\square_{0.09}MnO_3$ (bulk)[25]	352	1	0	1.78	—
$(RE_{MIX})_{0.67}Sr_{0.33}MnO_3$ (bulk)[78]	310	1	0	1.01	34
$La_{0.6}Dy_{0.07}Sr_{0.33}MnO_3$ (bulk)[79]	326	1	0	1.28	—
$La_{0.6}Dy_{0.07}Sr_{0.24}\square_{0.09}MnO_3$ (bulk)[79]	294	1	0	0.97	—
$Nd_{0.50}\square_{0.17}Sr_{0.33}MnO_3$ (19 nm)[80]	222	1	0	0.19	—
$Nd_{0.50}\square_{0.17}Sr_{0.33}MnO_3$ (33 nm)[80]	275	1	0	1.65	—
$(Sm_{0.8}Nd_{0.2})_{0.52}Sr_{0.48}MnO_3$ (bulk)[81]	136	1	0	2.87	—
$(Sm_{0.8}Nd_{0.2})_{0.52}Sr_{0.48}MnO_3$ (bulk)[81]	165	1	1.17	1.24	—
$La_{0.95}Na_{0.05}MnO_3$ (bulk)[82]	249	1	0	2.85	150
$La_{0.95}Na_{0.05}MnO_3$ (bulk)[82]	267	1	1.1	2.62	149
$La_{0.9}Na_{0.1}MnO_3$ (bulk)[82]	269	1	0	1.72	161
$La_{0.9}Na_{0.1}MnO_3$ (bulk)[82]	286	1	1.1	2.35	150
$La_{0.7}Ca_{0.3}MnO_3$ (bulk)[83]	250	1	0	5.15	—
$La_{0.7}Ca_{0.3}MnO_3$ (bulk)[83]	268.5	1	1.1	2.66	—
Gd (bulk)[84]	293	1.5	0	4.20	—

smaller values of the charge transfer resistance (R_{ct}) are beneficial for faster electron transport and may contribute to the OER activity. LMO shows the smallest R_{ct} in the 0.5 M K_2HPO_4 electrolyte. Based on this, it can be concluded that the LMO material potentially has higher catalytic activity in the K_2HPO_4 electrolyte than those in the 0.5 M K_2SO_4 and 0.1 M $K_2B_4O_7$ electrolytes.

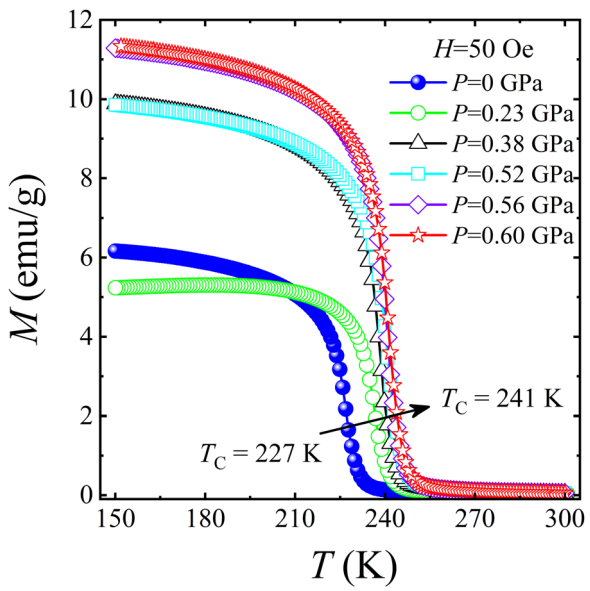

Fig. 6 Temperature dependences of magnetization $M_{FC}(T)$ at H = 50 Oe of LMO-1150 at different pressures.

The cyclic voltammogram (CV) tests performed at different scan rates show that the behavior of electrodes based on prepared samples is significantly diverse in different electrolytes. For 0.5 M K_2SO_4 and 0.5 M K_2HPO_4 electrolytes, two distinct peaks are observed on the CV curves (Fig. S8 and S9, ESI†) which correspond to reversible transitions of $Mn^{2+} \leftrightarrow Mn^{3+}$ (see Fig. 8(a)). At scan rates of 1 and 10 mV s^{-1}, the maxima of redox peaks are within the potential window from 1.67 to 1.42 V ($Mn^{2+} \leftrightarrow Mn^{3+}$, *vs.* RHE, Fig. S8, ESI†) and from 1.23 to 0.98 V ($Mn^{2+} \leftrightarrow Mn^{3+}$, *vs.* RHE, Fig. S9, ESI†) for 0.5 M K_2SO_4 and 0.5 M K_2HPO_4, respectively. Moreover, an increase in the scan rate to 50 mV s^{-1} leads to an enlargement in the interval between redox peaks. In addition, the very weak peaks of CV curves around 1.8 V can be observed due to the $Mn^{4+} \rightarrow Mn^{3+}$ transition (see Fig. 9(a)). In contrast to those described, the CV curves do not include clear redox peaks at scan rates from 1 to 50 mV s^{-1} in the 0.1 M $K_2B_4O_7$ electrolyte (Fig. S10, ESI†).

A subsequent linear sweep voltammetry (LSV) measurement at a scan rate of 1 mV s^{-1} is shown in Fig. 9(b). For all electrodes, OER activity is clearly observed at a value of more than 1.5 V. However, the OER overpotential values varied significantly with different electrolytes (Table S3, ESI†). The LSV results of the LMO materials at current densities of 5 and 10 mA cm^{-2} are shown in a diagram (see Fig. 9(d)). The OER overpotential is significantly lower when the 0.5 M K_2HPO_4

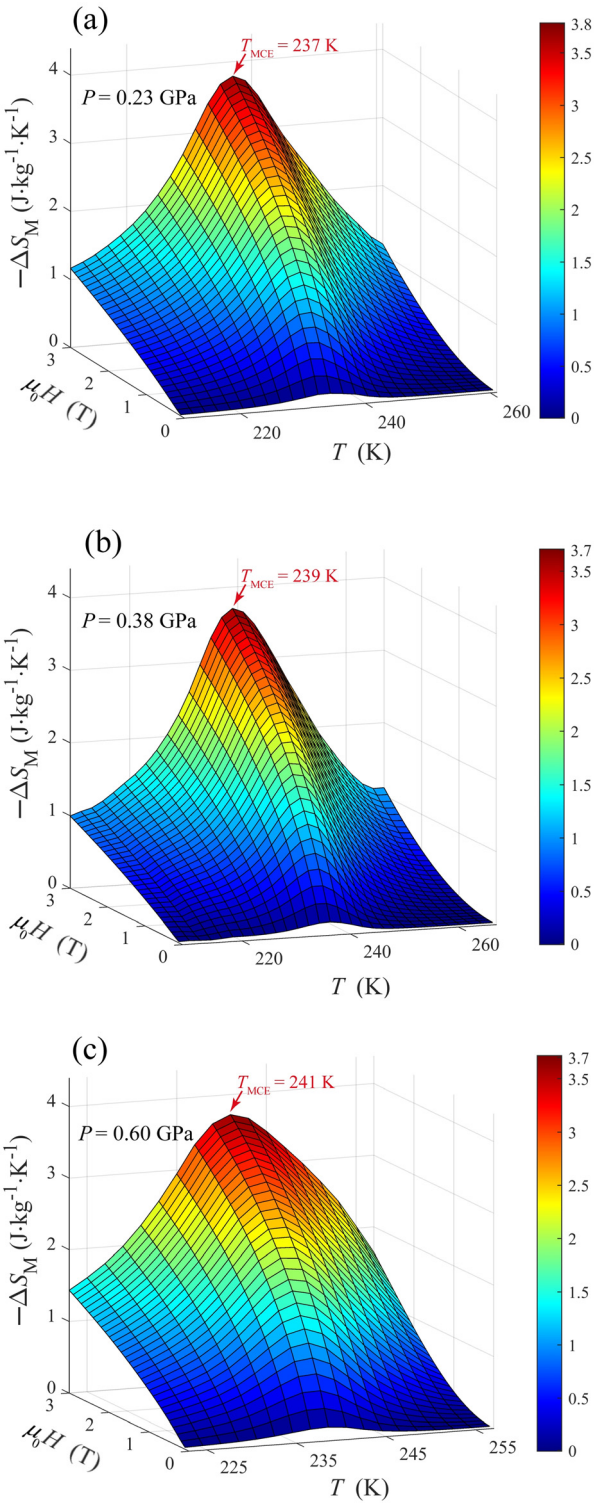

Fig. 7 Evolution of the magnetic entropy change $\Delta S_M(T, \mu_0 H)$ of LMO-1150 depending on the temperature and magnetic field at different P = 0.23 (a), 0.38 (b), and 0.60 GPa (c).

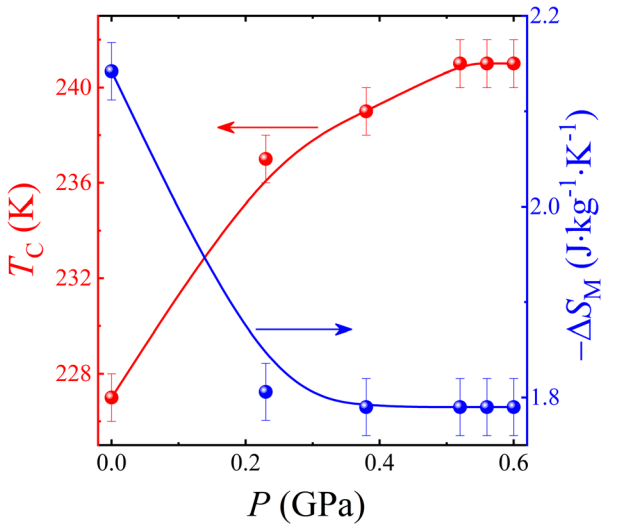

Fig. 8 Pressure-induced dependences of the Curie temperature T_C and magnetic entropy change ΔS_M (1 T) of LMO-1150.

electrolyte is used. Thus, the catalytic activity is largely influenced by the nature of the electrolyte rather than the post-annealing temperature of the LMO sample. This conclusion is in good agreement with the results of CP tests at a current density of 10 mA cm^{-2} (see Fig. 9(c)). During continuous electrolysis, the OER of the overpotential increases in different ways: (i) when using a 0.1 M $K_2B_4O_7$ solution, the potential gradually increases from 2.2 to 2.5 V for 6 h; (ii) in the case of the 0.5 M K_2HPO_4 electrolyte, the potential is fairly stable (up to 2.05 V) for 7 h and then increases rapidly; (iii) for a 0.5 M K_2SO_4 solution, the voltage first increases to about 2.25 V for 2 h, then decreases to 2.2 V and begins to increase rapidly after 7 h. This indicates a different type of interaction between the electrolytes and LMO. To clarify this issue, we examined the electrodes after CP tests.

According to the XRD results, the crystalline phase $K_{10}La_2(SO_4)_8$ was uniquely detected on the surface of the electrode after the CP test in the 0.5 M K_2SO_4 electrolyte (as an inclusion to the initial LMO phases, Fig. S11, ESI†). The crystal formation of $K_{10}La_2(SO_4)_8$ is also clearly seen in the SEM images (see insets in Fig. S11, ESI†). The obtained result is in good agreement with EDS and elemental mapping of the electrode surface (Fig. S12, ESI†). It can be seen that the crystallization of complex sulfate $K_{10}La_2(SO_4)_8$ occurs, and manganese compounds pass into an amorphous state since the LMO materials react with the electrolyte during electrolysis. Moreover, we additionally defined the influence of electrocatalysis on the magnetic properties of the LMO samples (Fig. S13, ESI†). As turned out, the magnitude of magnetization M after electrocatalysis decreases and strongly depends on the duration of the OER process, whereas T_C remains the same. For example, after 8 h of electrocatalysis in the K_2SO_4 (0.5 M) media at 10 mA cm^{-2}, the relative change in the magnetization $\Delta M/M$ reduces by 16% for LMO-1150 and 15% for LMO-1450 that is in good agreement with the mass loss before and after electrochemistry. This means that the FM interactions do not change during electrocatalysis, but the number of Mn ions decreases, which indicates a layer-by-layer dissolution of the electrode. In this connection, the significant increase in the overpotential OER after the 6 h CP test is the result of the destruction of the LMO catalysts (see Fig. 9(c)). It should be noted that a similar

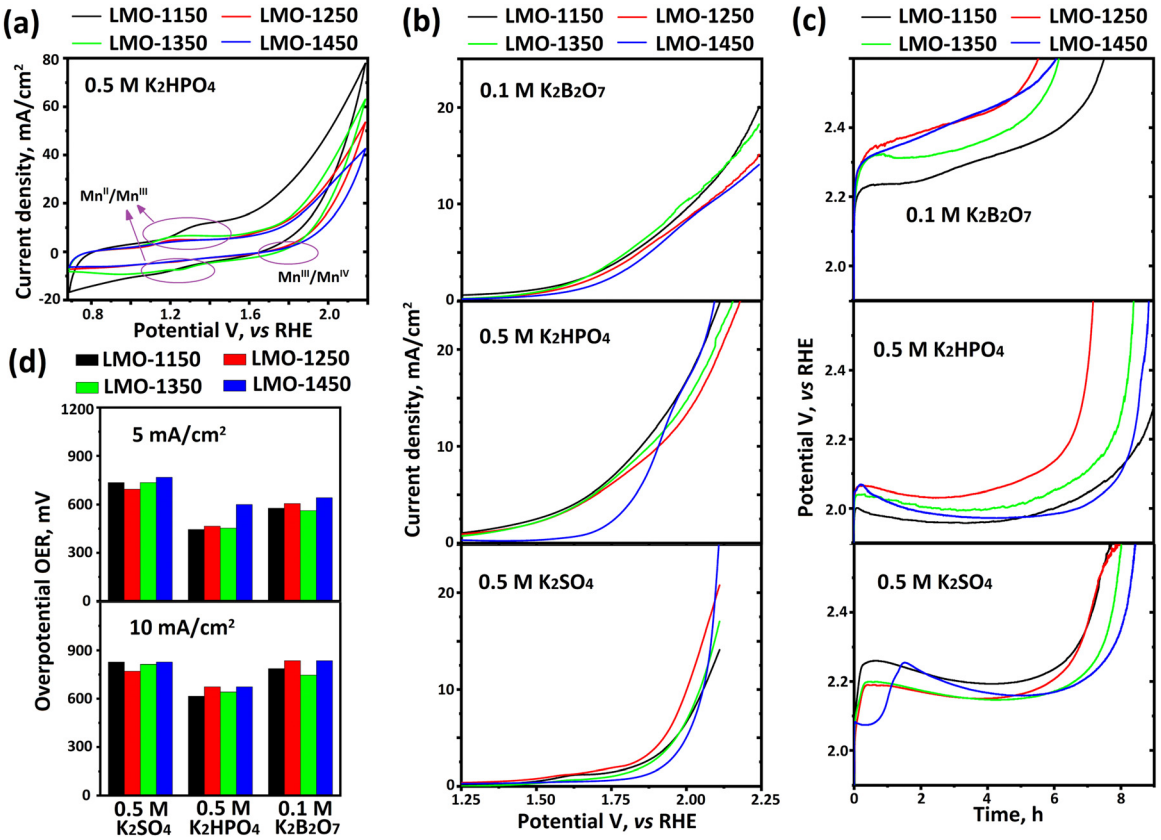

Fig. 9 Electrochemical testing of the LMO electrodes: CV curves at different scan rates in the 0.5 M KH_2PO_4 electrolyte (a). LSV curve plots at a scan rate of 1 mV s^{-1} in different electrolytes (b). Long-term CP test at a current density of 10 mA cm^{-2} in different electrolytes (c). LSV results at current densities of 5 and 10 mA cm^{-2} as a diagram for different electrolytes (d).

pathway for the transformation of LaSr-manganite (the formation of complex lanthanum sulfates) was observed earlier in the Na_2SO_4 electrolyte.[18]

Another way of the transformation of the LMO catalysts was observed after CP tests in 0.1 M $K_2B_4O_7$ and 0.5 M KH_2PO_4 mediums. The XRD results reveal the retention of the initial crystalline phases for the LMO samples, and no emergence of new compounds was found. However, the SEM images show changes on the surface of the catalysts (Fig. S14 and S15, ESI†). In the case of the 0.1 M $K_2B_4O_7$ electrolyte, bunches of nanoparticles are formed on the surface of the LMO catalyst (Fig. S14, ESI†). The EDS and elemental mapping results show surface potassium and boron contents. This suggests that during the CP test, the electrolyte interacts with the LMO materials, and amorphous particles of complex borates are formed on the surface. A gradual increase in the number of particles on the surface decreases the interface electrolyte–catalyst and gradually increases the OER of the overpotential (see Fig. 9(c)). In general, borate-based catalytic coatings can also provide high OER efficiency and stability of the OER in the 0.1 M $K_2B_4O_7$ electrolyte,[96,97] but here it was not observed. The changes on the surface of the LMO samples also occurred in the 0.5 M KH_2PO_4 electrolyte. However, the growth of nanoflowers on the surface was observed (see Fig. S15, ESI†). According to the EDS and elemental mapping, significant amounts of phosphorus and potassium were found on the surface of the electrodes (see Fig. S15, ESI†). This shows that the nature of the interaction of the phosphate electrolyte with surfaces of the LMO type is different in comparison with those described above. It is known that d-metal phosphates are effective electrocatalysts for the OER process in water splitting.[98] Thus, during electrolysis, phosphate compounds can be converted *in situ* to various forms of electrocatalysts.[98–100] Moreover, phosphates are good co-catalysts for the OER.[101] This is also evidenced by the results obtained here: the overpotential of the LMO materials for the OER process in the 0.5 M KH_2PO_4 electrolyte is minimal (see Fig. 9(c)). However, the formation of dense phosphate-based coatings can also harm OER effectiveness, which will be manifested after 6–7 hours of electrolysis (see Fig. 9(c)).

In summary, the nature of the electrolyte has a decisive influence on the electrochemical behavior of Mn-containing perovskites. Accordingly, these issues require further closer study for effective practical manganites in various electrochemical applications.

4. Conclusions

The structural, microstructural, magnetic, magnetocaloric, and electrochemical properties of the LMO ceramics obtained at

different annealing temperatures t_{ann} = 1150, 1250, 1350, and 1450 °C have been studied comprehensively. All ceramic samples are crystallized in a perovskite structure with a different type of symmetry: the rhombohedral $R\bar{3}c$ and/or the orthorhombic *Pnma* one. An increase in t_{ann} leads to the growth of the crystallite size, a decrease in the oxygen content, and a reduction in the tolerance factor of LMO which affect their magnetic properties. It has been found that with the increasing t_{ann} from 1150 to 1450 °C the FM phase content and the Curie temperature decrease dramatically from $M_S(T = 2\ K) = 68$ to 21 emu g^{-1} and from T_C = 227 to 113 K, respectively, because of the weakening of both the FM DE and multiple DE interactions by the structural imperfections. In addition, after electrocatalysis, the LMO ceramics show reduced values of M and stabilized T_C indicating a layer-by-layer loss of LMO depending on the duration of the OER and the persistence of FM DE interactions, respectively. Among all samples, LMO-1150 shows the highest magnetic entropy change $-\Delta S_M^{max} = 3.50$ J $(kg\ K)^{-1}$ under 1 T at T_C = 227 K with an optimal order/disorder ratio. At the applied external hydrostatic pressure, T_C is shifted towards higher temperature achieving ΔT_C = 14 K. At the same time, LMO-1150 saturates easily in both the MCE and T_C at a relatively low-pressure P of $\approx$ 0.4 GPa. The hydrostatic pressure makes the sample more magnetically homogeneous, expands the bandwidth W, increases significantly T_C, and reduces slightly ΔS_M through the modification of MnO_6 octahedra by increasing Mn–O–Mn bond angles and decreasing Mn–O bond distances. Moreover, the electrochemical testing of the prepared LMO samples has shown that the type of electrolyte significantly affects their electrocatalytic efficiency and stability for the OER. This is due to the different material–electrolyte interactions during electrolysis. The OER overpotential in the 0.5 M K_2HPO_4 electrolyte is the smallest for all LMO samples (within 615–675 mV at current densities of 10 mA cm^{-2}), which may be associated with the appearance of phosphate co-catalysts on the LMO surface. Moreover, LMO after electrocatalysis shows a decrease in its M without changing T_C, which makes it possible to control the depletion of the electrodes and predict their working time. The obtained results demonstrate the ways for expanding the multifunctionality of the rare-earth manganite materials and improving their functional properties.

Author contributions

Zhiwei Gong: writing – original draft, data curation, investigation, and methodology. Wei Xu: data curation, investigation, and methodology. N. A. Liedienov: writing – review and editing, conceptualization, data curation, and investigation. D. S. Butenko: data curation, investigation, and methodology. I. V. Zatovsky: writing – review and editing, data curation, conceptualization, and investigation. I. A. Gural'skiy: data curation, investigation, and methodology. Ziyu Wei: data curation, investigation, and methodology. Quanjun Li: data curation, investigation, and methodology. Bingbing Liu: data curation, investigation, methodology, and supervision. Yu. A. Batman: data curation, investigation, and methodology. A. V. Pashchenko: data curation, investigation, and methodology. G. G. Levchenko: writing – review and editing and supervision.

Conflicts of interest

There are no conflicts to declare.

Acknowledgements

This work was financially supported by the National Key Research and Development Program of China (No. 2018YFA0305900) and the National Natural Science Foundation of China (11874172, U2032215 and 11634004).

References

1 S. Chatterjee, K. Das and I. Das, *Phys. Chem. Chem. Phys.*, 2022, **24**, 8233–8244.
2 B. Arun, V. R. Akshay and M. Vasundhara, *RSC Adv.*, 2019, **9**, 23598–23606.
3 E. Zubov, A. Pashchenko, N. Nedelko, I. Radelytskiy, K. Dyakonov, A. Krzyżewski, A. Ślawska-Waniewska, V. Dyakonov and H. Szymczak, *Low Temp. Phys.*, 2017, **43**, 1190–1195.
4 M. T. Colomer, A. Ortiz, V. López-Domínguez, J. M. Alonso and M. García, *J. Eur. Ceram. Soc.*, 2017, **37**, 3527–3533.
5 Z. B. Guo, Y. W. Du, J. S. Zhu, H. Huang, W. P. Ding and D. Feng, *Phys. Rev. Lett.*, 1997, **78**, 1142–1145.
6 T. Hotta and E. Dagotto, *Theory of Manganites*, Springer, 2004.
7 L. D. Mendonca, M. S. Murari and M. D. Daivajna, *Phys. Chem. Chem. Phys.*, 2020, **22**, 19888–19902.
8 D. R. Sree, S. K. Cholleti, S. G. Fard, C. G. Reddy, P. Y. Reddy, K. R. Reddy and G. R. Turpu, *J. Appl. Phys.*, 2010, **108**, 113917.
9 M. Wali, R. Skini, M. Khlifi, E. Dhahri and E. K. Hlil, *Dalton Trans.*, 2015, **44**, 12796–12803.
10 V. K. Pecharsky and K. A. Gschneidner Jr., *J. Magn. Magn. Mater.*, 1999, **200**, 44–56.
11 J. Makni-Chakroun, I. Sfifir, W. Cheikhrouhou-Koubaa, M. Koubaa and A. Cheikhrouhou, *J. Magn. Magn. Mater.*, 2017, **432**, 484–493.
12 W. Wang, H. B. Zhang, G. D. Lin and Z. T. Xiong, *Appl. Catal., B*, 2000, **24**, 219–232.
13 S. Jin, K. J. May, H. A. Gasteiger, J. B. Goodenough and S. H. Yang, *Science*, 2012, **43**, 1383–1385.
14 H. Arandiyan, H. Dai, J. Deng, Y. Liu, B. Bai, Y. Wang, X. Li, S. Xie and J. Li, *J. Catal.*, 2013, **307**, 327–339.
15 J. O. Bockris and T. Otagawa, *J. Phys. Chem.*, 1983, **87**, 2960–2971.
16 J. Kim, Y. Xi, K. C. Tsao, S. Fang and Y. Hong, *J. Am. Chem. Soc.*, 2014, **46**, 14646–14649.
17 L. Duranti, I. N. Sora, F. Zurlo, I. Luisetto, S. Licoccia and E. Di Bartolomeo, *J. Eur. Ceram. Soc.*, 2020, **40**, 4076–4083.

18 Z. Wei, A. V. Pashchenko, N. A. Liedienov, I. V. Zatovsky, D. S. Butenko, Q. Li, I. V. Fesych, V. A. Turchenko, E. E. Zubov, P. Y. Polynchuk, V. G. Pogrebnyak, V. M. Poroshin and G. G. Levchenko, *Phys. Chem. Chem. Phys.*, 2020, **22**, 11817–11828.
19 A. J. Millis, B. I. Shraiman and R. Mueller, *Phys. Rev. Lett.*, 1996, **77**, 175.
20 A. J. Millis, P. B. Littlewood and A. Shraiman, *Phys. Rev. Lett.*, 1995, **74**, 5144.
21 S. Mori, C. H. Chen and S. W. Cheong, *Phys. Rev. Lett.*, 1998, **81**, 3972.
22 N. A. Liedienov, V. M. Kalita, A. V. Pashchenko, Y. I. Dzhezherya, I. V. Fesych, Q. Li and G. G. Levchenko, *J. Alloys Compd.*, 2020, **836**, 155440.
23 P. Orgiani, A. Galdi, C. Aruta, V. Cataudella, G. De Filippis, C. A. Perroni, V. Marigliano Ramaglia, R. Ciancio, N. B. Brookes, M. Moretti Sala, G. Ghiringhelli and L. Maritato, *Phys. Rev. B*, 2010, **82**, 205122.
24 M. Wali, R. Skini, M. Khlifi, E. Dhahri and E. K. Hlil, *J. Magn. Magn. Mater.*, 2015, **394**, 207–211.
25 B. Arun, V. Akshay and M. Vasundhara, *Dalton Trans.*, 2018, **47**, 15512–15522.
26 E. Pollert, *J. Solid State Chem.*, 1980, **35**, 262–266.
27 D. Abou-Ras, A. Cheikh-Rouhou, J. Pierre, J.-P. Renard, L. Reversat and K. Shimizu, *J. Magn. Magn. Mater.*, 2001, **233**, 147–154.
28 P. Orgiani, C. Aruta, R. Ciancio, A. Galdi and L. Maritato, *J. Nanopart. Res.*, 2013, **15**, 1–9.
29 A. V. Pashchenko, V. K. Prokopenko, Yu. F. Revenko, A. A. Shemyakov and A. G. Sil'cheva, *Tech. Phys.*, 2012, **57**, 1508.
30 N. A. Liedienov, A. V. Pashchenko, V. K. Prokopenko, D. D. Tatarchuk, Y. F. Revenko, V. A. Turchenko, V. V. Burchovetskii, V. Y. Sycheva, A. G. Sil'cheva, Y. V. Didenko and G. G. Levchenko, *Low Temp. Phys.*, 2017, **43**, 1076–1085.
31 A. V. Pashchenko, V. P. Pashchenko, V. K. Prokopenko, Y. F. Revenko, Y. S. Prylipko, N. A. Ledenev, G. G. Levchenko, V. P. Dyakonov and H. Szymczak, *Acta Mater.*, 2014, **70**, 218–227.
32 A. V. Pashchenko, V. P. Pashchenko, Y. F. RevenKo, V. K. Prokopenko and L. G. Gusakova, *Metallofiz. Noveishie Tekhnol.*, 2010, **32**, 487–504.
33 A. V. Pashchenko, V. K. Prokopenko, Yu. F. Revenko, A. S. Mazur, V. V. Burchovetskii, V. A. Turchenko, N. A. Liedienov, V. G. Pitsyuga, G. G. Levchenko, V. P. Dyakonov and H. Szymczak, *J. Magn. Magn. Mater.*, 2016, **416**, 457–465.
34 A. V. Pashchenko, V. K. Prokopenko, Yu. F. Revenko, N. G. Kisel, V. I. Kamenev, A. G. Sil'cheva, N. A. Ledenev, V. V. Burkhovetskii and G. G. Levchenko, *Phys. Solid State*, 2014, **56**, 955–966.
35 A. V. Pashchenko, V. K. Prokopenko, Y. F. Revenko, A. S. Mazur, V. Y. Sycheva, V. V. Burkhoveckii, N. G. Kisel, A. G. Sil'cheva and N. A. Liedienov, *Low Temp. Phys.*, 2014, **40**, 717.
36 N. A. Liedienov, A. V. Pashchenko, V. P. Pashchenko, V. K. Prokopenko, Y. F. Revenko, A. S. Mazur, V. Y. Sycheva, V. I. Kamenev and G. G. Levchenko, *Low Temp. Phys.*, 2016, **42**, 1102–1111.
37 G. F. Wang, L. R. Li and X. F. Zhang, *J. Magn. Magn. Mater.*, 2016, **397**, 198–204.
38 M.-H. Phan, *J. Magn. Magn. Mater.*, 2007, **308**, 325–340.
39 A. E. R. T. AboZied, A. I. Ali and T. A. Salaheldin, *J. Magn. Magn. Mater.*, 2019, **479**, 260–267.
40 Z. Wei, N. A. Liedienov, Q. Li, A. V. Pashchenko, W. Xu, V. A. Turchenko, M. Yuan, I. V. Fesych and G. G. Levchenko, *Ceram. Int.*, 2021, **47**, 24553–24563.
41 C. Ritter, M. Ibarra, J. De Teresa, P. Algarabel, C. Marquina, J. Blasco, J. Garcia, S. Oseroff and S. Cheong, *Phys. Rev. B: Condens. Matter Mater. Phys.*, 1997, **56**, 8902.
42 A. V. Pashchenko, V. P. Pashchenko, N. A. Liedienov, V. K. Prokopenko, Y. F. Revenko, N. E. Pismenova, V. V. Burhovetskii, V. Y. Sycheva, A. V. Voznyak, G. G. Levchenko, V. P. Dyakonov and H. Szymczak, *J. Alloys Compd.*, 2017, **709**, 779–788.
43 A. V. Pashchenko, N. A. Liedienov, V. P. Pashchenko, V. K. Prokopenko, V. V. Burhovetskii, A. V. Voznyak, I. V. Fesych, D. D. Tatarchuk, Y. V. Didenko, A. I. Gudymenko, V. P. Kladko, A. A. Amirov and G. G. Levchenko, *J. Alloys Compd.*, 2018, **767**, 1117–1125.
44 H. Rietveld, *J. Appl. Crystallogr.*, 1969, **2**, 65–71.
45 B. H. Toby and R. B. Von Dreele, *J. Appl. Crystallogr.*, 2013, **46**, 544–549.
46 V. Dyakonov, *Instrum. Exp. Tech.*, 1983, **5**, 5236–5240.
47 M. Yuan, G. Levchenko, Q. Li, L. Berezhnaya, H. Fylymonov, A. B. Gaspar, M. Seredyuk and J. A. Real, *Inorg. Chem.*, 2020, **59**, 10548–10556.
48 B. Vertruyen, J. F. Fagnard, P. Vanderbemden, M. Ausloos, A. Rulmont and R. Cloots, *J. Eur. Ceram. Soc.*, 2007, **27**, 3923–3926.
49 N. Abdelmoula, K. Guidara, A. Cheikh-Rouhou, E. Dhahri and J. C. Joubert, *J. Solid State Chem.*, 2000, **151**, 139–144.
50 A. M. De Léon-Guevara, P. Berthet, J. Berthon, F. Millot, A. Revcolevschi, A. Anane, C. Dupas, K. Le Dang, J. P. Renard and P. Veillet, *Phys. Rev. B*, 1997, **56**, 6031.
51 H. Y. Hwang, S. W. Cheong, P. G. Radaelli, M. Marezio and B. Batlogg, *Phys. Rev. Lett.*, 1995, **75**, 914–917.
52 **https://abulafia.mt.ic.ac.uk/shannon/ptable.php**.
53 S. Othmani, M. Bejar, E. Dhahri and E. K. Hlil, *J. Alloys Compd.*, 2009, **475**, 46–50.
54 S. Ridha, D. Essebti and E. Hlil, *Crystals*, 2017, **7**, 1–12.
55 V. Markovich, A. Wisniewski and H. Szymczak, *Handb. Magn. Mater.*, 2014, **22**, 1–201.
56 W. H. Meiklejohn and C. P. Bean, *Phys. Rev.*, 1956, **102**, 1413.
57 H. Ohldag, A. Scholl, F. Nolting, E. Arenholz, S. Maat, A. T. Young, M. Carey and J. Stohr, *Phys. Rev. Lett.*, 2003, **91**, 017203.
58 A. V. Pashchenko, V. P. Pashchenko, V. K. Prokopenko, V. A. Turchenko, Y. F. Revenko, A. S. Mazur, V. Y. Sycheva, N. A. Liedienov, V. G. Pitsyuga and G. G. Levchenko, *J. Exp. Theor. Phys.*, 2017, **124**, 100–113.

59 V. Dyakonov, A. Ślawska-Waniewska, N. Nedelko, E. Zubov, V. Mikhaylov, K. Piotrowski, A. Szytuła, S. Baran, W. Bazela, Z. Kravchenko, P. Aleshkevich, A. Pashchenko, K. Dyakonov, V. Varyukhin and H. Szymczak, *J. Magn. Magn. Mater.*, 2010, **322**, 3072–3079.
60 R. C. Sahoo, S. Das, S. K. Giri, D. Paladhi and T. K. Nath, *J. Magn. Magn. Mater.*, 2019, **469**, 161–170.
61 I. N. Bhatti, I. N. Bhatti, R. N. Mahato and M. A. H. Ahsan, *Phys. Lett. A*, 2019, **383**, 2326–2332.
62 M. H. Khan, A. Roychowdhury, D. Das and S. Pal, *J. Alloys Compd.*, 2015, **650**, 328–335.
63 A. Ulyanov, N. Pismenova, D. Yang, V. Krivoruchko and G. Levchenko, *J. Alloys Compd.*, 2013, **550**, 124–128.
64 J. Vergara, R. J. Ortega-Hertogs, V. Madurga, F. Sapina, Z. El-Fadli, E. Martinez, A. Beltran and K. V. Rao, *Phys. Rev. B: Condens. Matter Mater. Phys.*, 1999, **60**, 1127–1135.
65 N. A. Liedienov, Z. Wei, V. M. Kalita, A. V. Pashchenko, Q. Li, I. V. Fesych, V. A. Turchenko, C. Hou, X. Wei, B. Liu, A. T. Kozakov and G. G. Levchenko, *Appl. Mater. Today*, 2022, **26**, 101340.
66 A. M. Tishin and Y. I. Spichkin, *The magnetocaloric effect and its applications*, CRC Press, 2016.
67 V. Pecharsky, K. Gschneidner Jr., A. Pecharsky and A. Tishin, *Phys. Rev. B: Condens. Matter Mater. Phys.*, 2001, **64**, 144406.
68 P. S. Tola, H. S. Kim, D. H. Kim, T. L. Phan, J. S. Rhyee, W. H. Shon, D. S. Yang, D. H. Manh and B. W. Lee, *J. Phys. Chem. Solids*, 2017, **111**, 219–228.
69 A. Biswas, S. Chandra, M.-H. Phan and H. Srikanth, *J. Alloys Compd.*, 2012, **545**, 157–161.
70 S. Chandra, A. Biswas, S. Datta, B. Ghosh, V. Siruguri, A. K. Raychaudhuri, M.-H. Phan and H. Srikanth, *J. Phys.: Condens. Matter*, 2012, **24**, 366004.
71 S. Belhamra, R. Masrour, A. Jabar and E. K. Hlil, *Polyhedron*, 2021, **193**, 114891.
72 P. S. Tola, D. H. Kim, T. L. Phan, C. Liu and B. W. Lee, *J. Korean Phys. Soc.*, 2017, **69**, 65–71.
73 N. Tahiri, S. Dahbi, I. Dani, O. El Bounagui and H. Ez-Zahraouy, *Phase Transitions*, 2021, **94**, 826–834.
74 G. Muscas, K. Prabahar, F. Congiu, G. Datt and T. Sarkar, *J. Alloys Compd.*, 2022, **906**, 164385.
75 E. A. Hurtado-Aviles, M. Vila, J. J. Vilatela, H. Martines-Arano, J. Bornacelli, J. A. García-Merino, F. Cervantes-Sodi and C. Torres-Torres, *Phys. Chem. Chem. Phys.*, 2022, **24**, 1081–1090.
76 T.-L. Phan, P. Thanh, P. Yen, P. Zhang, T. Thanh and S. Yu, *Solid State Commun.*, 2013, **167**, 49–53.
77 R. Skini, M. Khlifi and E. K. Hlil, *RSC Adv.*, 2016, **6**, 34271.
78 B. Arun, V. Akshay, G. R. Mutta, C. Venkatesh and M. Vasundhara, *Mater. Res. Bull.*, 2017, **94**, 537–543.
79 M. Mukesh, B. Arun, V. Akshay and M. Vasundhara, *New J. Chem.*, 2020, **44**, 13480–13487.
80 B. Arun, V. Akshay, K. D. Chandrasekhar, G. R. Mutta and M. Vasundhara, *J. Magn. Magn. Mater.*, 2019, **472**, 74–85.
81 S. Arumugam, P. Sarkar, P. Mandal, A. Murugeswari, K. Matsubayashi, C. Ganguli and Y. Uwatoko, *J. Appl. Phys.*, 2010, **107**, 113904.
82 R. Das, A. Midya, M. Kumari, A. Chaudhuri, X. Yu, A. Rusydi and R. Mahendiran, *J. Phys. Chem. C*, 2019, **123**, 3750–3757.
83 R. Szymczak, R. Kolano, A. Kolano-Burian, J. Pietosa and H. Szymczak, *J. Magn. Magn. Mater.*, 2010, **322**, 1589–1591.
84 W. Zhong, W. Chen, W. Ding, N. Zhang, A. Hu, Y. Du and Q. Yan, *J. Magn. Magn. Mater.*, 1999, **195**, 112–118.
85 R. Rao, Y. Han, X. Kan, X. Zhang, M. Wang, N. Qian, G. Zheng and Y. Ma, *J. Alloys Compd.*, 2020, **837**, 155476.
86 R. Das, A. Midya, M. Kumari, A. Chaudhuri, X. Yu, A. Rusydi and R. Mahendiran, *J. Phys. Chem. C*, 2019, **123**, 3750–3757.
87 X. Zhang, Y. Han, X. Kan, M. Wang, R. Rao, G. Zheng and Y. Ma, *J. Am. Ceram. Soc.*, 2021, **104**, 955–965.
88 C. Jin, X. Cao, L. Zhang, C. Zhang and R. Yang, *J. Power Sources*, 2013, **241**, 225–230.
89 K. A. Stoerzinger, M. Risch, J. Suntivich, W. M. Lü, J. Zhou, M. D. Biegalski, H. M. Christen, Ariando, T. Venkatesan and Y. Shao-Horn, *Energy Environ. Sci.*, 2013, **6**, 1582–1588.
90 J. Du, T. Zhang, F. Cheng, W. Chu, Z. Wu and J. Chen, *Inorg. Chem.*, 2014, **53**, 9106–9114.
91 M. Risch, K. A. Stoerzinger, S. Maruyama, W. T. Hong, I. Takeuchi and Y. Shao-Horn, *J. Am. Chem. Soc.*, 2014, **136**, 5229–5232.
92 T. Li, J. Liu, X. Jin, F. Wang and Y. Song, *Electrochim. Acta*, 2016, **198**, 115–126.
93 J. Scholz, M. Risch, K. A. Stoerzinger, G. Wartner, Y. Shao-Horn and C. Jooss, *J. Phys. Chem. C*, 2016, **120**, 27746–27756.
94 D. S. Butenko, S. Li, V. O. Kotsyubynsky, V. M. Boychuk, V. I. Dubinko, P. I. Kolkovsky, N. A. Liedienov, N. I. Klyui, W. Han and I. V. Zatovsky, *Int. J. Hydrogen Energy*, 2021, **46**, 21462.
95 Y. Z. Vassilyeva, D. S. Butenko, S. Li, W. Han and A. Y. Pak, *Mater. Chem. Phys.*, 2020, **254**, 123509.
96 L. Xie, R. Zhang, L. Cui, D. Liu, S. Hao, Y. Ma, G. Du, A. M. Asiri and X. Sun, *Angew. Chem., Int. Ed.*, 2017, **56**, 1064–1068.
97 C. You, Y. Ji, Z. Liu, X. Xiong and X. Sun, *ACS Sustainable Chem. Eng.*, 2018, **6**, 1527–1531.
98 R. Guo, X. Lai, J. Huang, X. Du, Y. Yan, Y. Sun, G. Zou and J. Xiong, *ChemElectroChem*, 2018, **5**, 3822–3834.
99 I. V. Odynets, N. Y. Strutynska, J. Li, W. Han, I. V. Zatovsky and N. I. Klyui, *Dalton Trans.*, 2018, **47**, 15703–15713.
100 C. Mu, D. S. Butenko, I. V. Odynets, I. V. Zatovsky, J. Li, W. Han and N. I. Klyui, *Dalton Trans.*, 2020, **49**, 8226–8237.
101 Y. Li and C. Zhao, *Chem. Mater.*, 2016, **28**, 5659–5666.